

Adaptive Shape Ripening and Interparticle Bridging of L-Arginine-Stabilized Silica Nanoparticles during Evaporative Colloidal Crystal Assembly

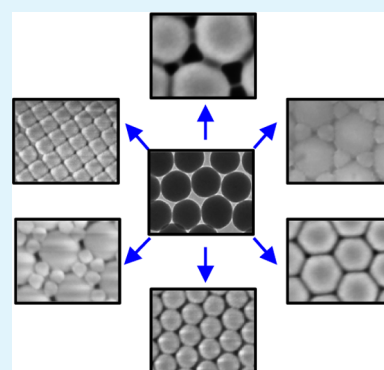
Jennifer L. Russell, Ngoc-Lan L. Tran, and Thomas E. Mallouk*^{ID}

Departments of Chemistry, Biochemistry and Molecular Biology, and Physics, The Pennsylvania State University, University Park, State College, Pennsylvania 16802, United States

S Supporting Information

ABSTRACT: During evaporative self-assembly of colloidal crystal films, spherical L-arginine-stabilized silica colloids adapt to different close-packed geometries by faceting and forming bridge connections with their nearest neighbors. We systematically studied the morphological changes of 37 and 138 nm diameter colloids during evaporative assembly and compared them to 65 nm Stöber silica colloids prepared without L-arginine. Colloidal crystal films were grown from particles that had been dialyzed against water or L-arginine, and tetraethyl orthosilicate (TEOS) and/or L-arginine were added to solutions during colloidal film growth. Solid-state ²⁹Si NMR spectra showed the presence of L-arginine and incompletely condensed silica in colloids grown from silica seeds in L-arginine solutions. These colloids were especially susceptible to chemical ripening during the colloidal assembly process, adopting faceted shapes that reflected the packing symmetry of the colloidal crystal films. The addition of L-arginine and TEOS accelerated these shape changes by catalyzing the hydrolysis and olation of silica and by adding a source of silica to the solution, respectively. This chemistry provides a route to single-component and binary colloidal crystals composed of nonspherical silica building blocks.

KEYWORDS: silica nanoparticles, colloids, evaporative self-assembly, colloidal crystal, L-arginine



INTRODUCTION

Colloidal crystal assembly provides a flexible pathway for achieving structural and compositional control of three-dimensionally ordered nanomaterials. Colloidal crystals can be made from a broad range of material classes (e.g., semiconductors, metals, and polymers) and fall within a size regime that is useful for applications such as photonics, microfluidics, magnetism, catalysis, sensing, or fundamental studies of crystal growth.^{1–11} In addition to the size and composition of their component colloids, colloidal shape is a significant factor in determining the packing fraction and crystal structure of the assembled particles, as well as their collective physical and electronic properties. Nanoparticle shapes beyond spheres and highly symmetric polyhedra can in principle provide access to a broader range of structures and functionality in colloidal crystals.^{12–17}

While silica and polymer colloidal crystals are typically grown from spherical particles, several groups have explored methods for introducing asymmetry into colloids by direct synthesis, sintering, etching, or templating.^{16–20} For example, Velikov and co-workers irradiated silica and zinc sulfide photonic crystals to deform the particle aspect ratios, which in turn shifted their optical properties.¹⁶ In addition to methods that involve assembly of asymmetric colloids or postprocessing of colloidal crystals made from spherical colloids, the lowering of particle symmetry may also occur during the process of

nanoparticle self-assembly itself. While studying the vertical evaporative assembly of L-arginine-stabilized silica nanoparticles into colloidal crystal films, we observed morphological changes in the dried silica nanoparticles. These shape changes depend upon the local packing geometry as shown in several examples in Figure 1. These examples are representative of the types of shape anomalies found within larger samples, in which the extent of propagation varied from several hundred nanometers to millimeters. Loose particle packing, as in Figure 1a, typically yielded only spherical particles, but tight hexagonal packing (Figure 1b) yielded hexagonally faceted particles and square-type packing (also a loosely packed configuration) produced cube-shaped particles (Figure 1c). These shape changes persist after high temperature sintering (600–650 °C) and can be replicated into inverse opal structures when the colloidal crystals are infiltrated with other materials and the silica template is removed (Figure S1). Binary packing arrangements (mixtures of two different-sized particles) result in other striking shapes including rounded polyhedral structures such as ovaloids, tetrahedra, and teardrops (Figure 1d–h). This adaptive shape-ripening phenomenon presents additional complexity in understanding

Received: October 13, 2018

Accepted: January 8, 2019

Published: January 8, 2019

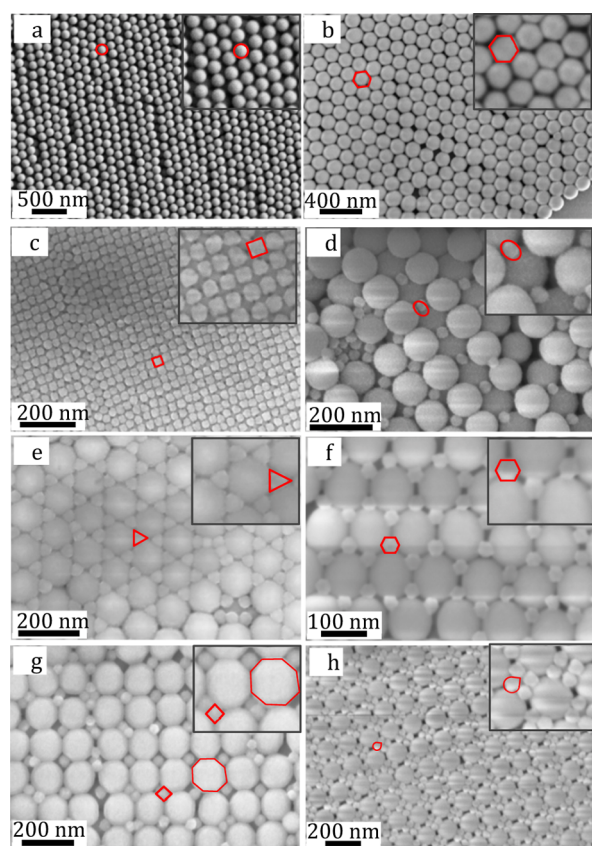


Figure 1. Shape anisotropy in films of *L*-arginine-stabilized silica nanoparticles. (a) Spherical particles in a unary lattice, (b) hexagonal in a unary lattice, (c) cubic in a unary lattice, (d) oblong in a binary lattice, (e) tetrahedral in a binary lattice, (f) hexagonal in a binary lattice, (g) octagonal and tetrahedra in a binary lattice, and (h) tear drop-shaped small particles in a binary lattice. The as-prepared silica sols were diluted 7.5–10 times in water and assembled as films on Si wafers by vertical evaporation at 40 °C in 85% relative humidity.

the assembly of silica nanoparticles and the implications it has for colloidal film properties as they deviate from the simple packing structures of spherical hard spheres. With sphere assemblies that are periodic on the optical length scale, changes in particle shape are expected to change the properties of photonic crystals and optical devices derived from them. Unary and binary crystals of silica spheres are also used as templates to prepare polymer, metal, semiconductor, and ceramic replicas, the physical properties of which are strongly affected by the geometry of the template. Understanding the phenomenon of shape ripening is thus potentially relevant to predicting and controlling the properties of these inverse opal materials.

Several mechanisms may contribute to shape changes in silica nanoparticles during colloidal crystal assembly. One possible factor is capillary-induced deformation. During evaporative film growth, particles at the air–water–substrate interface are drawn together by capillary forces as the thin liquid meniscus line in the voids between particles recedes (drying). Through the combination of interfacial tension and the elastic modulus of the particles, deformation may occur at the particle–particle interface to lower the total energy as the distance between particles closes. This space-filling shape deformation behavior is well documented in the process of softer latex and polymer film formation and sintering, but it is

not usually discussed in films made of harder materials such as silica.^{21–24} This mechanism is consistent with some of the shapes in Figure 1, as the number of facets in the polyhedral colloidal shapes corresponds to the number of nearest neighbors/interfaces.

However, as shown in Figure 2, there is evidence of additional, solution chemistry-driven factors that affect the

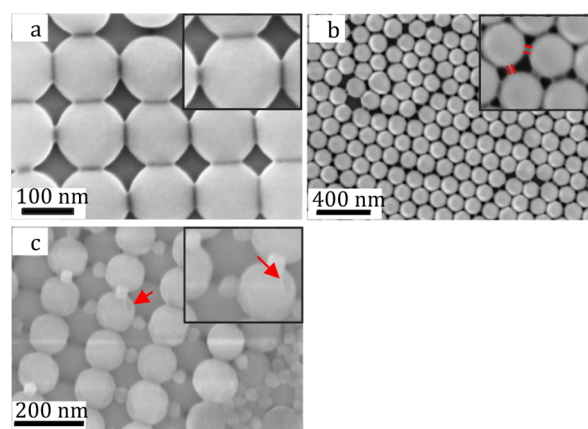


Figure 2. Examples of possible chemically driven morphological changes in *L*-arginine-stabilized silica nanoparticles. (a) Interparticle fusing, (b) bridging, and (c) deep indentations in film cross section. Colloid films were grown as described in Figure 1.

shape ripening of the nanoparticles. Figure 2a shows interfacial necking and fusing of nanoparticles that is reminiscent of arrested coalescence.^{24,25} Figure 2b depicts a striking example of particle bridging on a length scale of up to ~10 nm. The number of these extensions also reflects the nearest-neighbor symmetry of the particle site in the lattice. Figure 2c shows larger particles deeply notched where smaller particles that were once touching fell out during sample cleavage as shown by cross-sectional scanning electron microscopy (SEM). This sharp notching suggests that larger particles are either growing around contacted neighbors or localized dissolution is occurring. Upon close inspection of Figure 1f, the vertices of the hexagonally shaped smaller particles appear to be stretched extensions from the particles, much like the bridges in Figure 2b. These observations suggest “ripening” chemistry during evaporative deposition that sharpens or develops nanoparticle facets and facilitates interparticle bridging. Because the nanoparticles in Figures 1 and 2 were assembled as prepared without further purification, there are potentially reactive species in solution (underreacted soluble silicates, etc.) that could hydrolyze or condense as silicates during the deposition process.

In this study, we investigated the role of solution components and nanoparticle composition on the morphological changes of *L*-arginine-stabilized silica colloidal nanoparticles during evaporative assembly. Our hypothesis was that during the late stages of colloidal film drying, the combined presence of the base catalyst/stabilizer *L*-arginine and reactive silicate species [sourced from soluble particle species or unreacted tetraethyl orthosilicate (TEOS) reagent] sculpts facets and builds bridges that interconnect nanoparticles, driven by lowering the colloid surface energy and overall free energy of the colloidal crystal film. This hypothesis was tested by comparing films grown from the as-prepared and dialyzed colloidal solutions and then characterizing the product

Table 1. ICP–AES Data from Silica Colloid Dialysis

particle size (nm)	dialyzate	Si ppm 2 h	Si ppm 24 h	Si ppm 26 h
37	water	0.43 ± 0.00	0.79 ± 0.04	0.01 ± 0.01
37	3.3 mM L-arginine	0.71 ± 0.05	3.49 ± 0.07	0.69 ± 0.01
138	water	0.12 ± 0.00	0.27 ± 0.02	<0.01 ± 0.00
138	4.5 mM L-arginine	2.56 ± 0.00	8.39 ± 0.02	2.97 ± 0.01
65 (Stöber)	water	0.17 ± 0.02	2.72 ± 0.06	0.51 ± 0.01
65 (Stöber)	4.5 mM L-arginine	0.16 ± 0.01	3.28 ± 0.13	0.75 ± 0.05
N/A	water blank	<0.01 ± 0.00	<0.01 ± 0.00	<0.01 ± 0.00
N/A	4.5 mM L-arginine blank	0.01 ± 0.00	0.04 ± 0.00	0.01 ± 0.01

composition and morphology by solid-state NMR and electron microscopy. By studying nanoparticle composition changes, we hoped to elucidate the solution or compositional “softening” factors that could facilitate particle deformation. L-Arginine and silicate precursors were also added to the colloidal deposition solutions to determine their cumulative effects during deposition and recreate some of the film and nanoparticle behaviors obtained without dialysis. Comparisons were also made with silica colloids synthesized without L-arginine by the Stöber synthetic method.

EXPERIMENTAL METHODS

Silica Colloid Synthesis. Silica nanoparticles of 37.2 ± 3.0 nm diameter were prepared by following the method of Hartlen et al.²⁶ Approximately 20 nm diameter silica seeds were prepared by gently stirring a mixture of 0.52 mmol L-arginine (Sigma-Aldrich, $\geq 98\%$) and 3.8 mol nanopure water (18.2 M Ω cm, Barnstead) below a floating layer of 0.042 mol cyclohexane (Sigma-Aldrich, anhydrous, 99.5%) and 0.025 mol TEOS (Sigma-Aldrich, 98%). This biphasic mixture was reacted in a sealed flask for 20 h at 60 °C. Nanoparticles of 37 nm diameter were then prepared by mixing 20 mL of the seeds with 4.0 mol water and with a floating layer of 0.031 mol TEOS and 0.093 mol cyclohexane. This mixture was further reacted for 30 h at 60 °C. Following this step, solutions were allowed to cool to room temperature, and then, the aqueous phases containing the colloids were collected via pipet after the organic supernatant was first siphoned off by pipet. Water used in this and other experiments was deionized to 18.2 M Ω cm using a Barnstead Nanopure system.

The 137.9 ± 5.7 nm diameter silica colloids were prepared by a slight modification of the method reported by Watanabe et al.²⁷ Seed particles (14 nm) were synthesized by rapidly mixing 4.8 mol water, 0.5 mmol L-arginine, and 25 mmol TEOS at 70 °C for 24 h. The 14 nm seeds were then grown to 138 nm in 24 h by mixing 0.26 g of seeds in 1.1 mol water, 1.5 mol ethanol (Koptec, 200 proof, anhydrous), 0.5 mmol L-arginine, and 25 mmol TEOS at 70 °C.

Additionally, 65.3 ± 8.4 nm diameter silica particles were synthesized by a modified Stöber method without the addition of L-arginine. These colloids were prepared by mixing 50 mL of ethanol, 3 mL of aqueous ammonia solution (28–30%, Sigma-Aldrich), and 1.5 mL of TEOS at room temperature for 24 h under rapid stirring.²⁸

Dialysis of Colloidal Suspensions. Colloids were purified at room temperature under constant stirring using Spectra/Por 3.5 kDa cellulose dialysis tubing in 100 times volume dialyzate, which was either water or an L-arginine buffered solution (4.5 mM L-arginine dialyzate for 65 and 138 nm diameter and 3.3 mM for 37 nm diameter silica colloids). The differences in L-arginine concentration for 37 and 138 nm colloids were based on the initial concentration of the amino acid in each synthesis. Solvent exchanges were carried out after 2 h and then 24 h every day for 4 days.

Film Deposition. Colloidal crystal films were fabricated by vertical evaporation.^{29,30} Dry, cleaned silicon wafer substrates were slanted approximately 30° from the vertical direction in open plastic cylindrical vials. Each vial was filled with colloidal suspension and then placed a humidity- and temperature-controlled oven at 40 °C and approximately 85% humidity. The humidity was regulated by using a

crystallizing dish containing a saturated salt solution as previously described.³⁰

Characterization. Colloidal particles were sized (>100 nanoparticles counted for statistics) and films were imaged by SEM using Zeiss SIGMA VP-FESEM. We imaged all films without the use of metal coatings. Transmission electron microscopy (TEM) micrographs were obtained on JEOL 1200 TEM. Solid-state CPMAS NMR studies were performed on a Bruker AVANCE-III-HD-500 MHz or Bruker AVANCE-300 MHz. For NMR studies, colloidal sols were evaporated and collected as bulk powders. Some powders were granular and were ground to prepare them for solid-state NMR experiments. Inductively coupled plasma atomic emission spectroscopy (ICP–AES) analyses of colloidal solution dialyzates were collected in triplicate using a PerkinElmer Optima 5300 instrument.

RESULTS AND DISCUSSION

Dialysis of Silica Colloidal Solutions. In order to investigate the chemical reactions driving colloidal shape changes during assembly, solutions of arginine-stabilized 37 and 138 nm diameter silica nanoparticles were first purified by dialysis. These nanoparticle sizes were chosen based on their tendency to crystallize in several different packing arrangements when codeposited, thus providing different local geometries for the study of shape ripening. The binary crystal phase(s) is established by the size ratio and particle concentrations. With the sphere sizes and conditions used here, AB₂ and to a lesser extent AB₁₃ and AB crystal structures were obtained. The 37 nm particles were closer in size to the 20 nm seeds from which they were grown, whereas the 138 nm particles underwent significant seed regrowth relative to their 14 nm seeds. Colloidal sols were dialyzed against water, as well as against L-arginine in approximately the same concentration as in their synthesis. These L-arginine dialyzate solutions were expected to be more concentrated in L-arginine than the originally prepared particle solutions as some of the free L-arginine associates with or is possibly encapsulated by the nanoparticles during synthesis. L-Arginine incorporation has been discussed elsewhere.^{31–34} The purpose of performing dialysis in water was to determine the effects of removing L-arginine, soluble silicates, and unreacted TEOS, as well as ethanol or residual cyclohexane (37 nm silica only). Conversely, dialysis against an L-arginine solution removes these residual components from the colloid solutions without removing all of the free and surface-associated L-arginine. Regardless of the dialyzate used, the dialysis bags of 138 nm colloidal solutions swelled nearly three times in volume within the first several hours, likely because of the volume exclusion effect.³⁵ The smaller 37 nm colloids did not discernibly change the volume during dialysis.

The first three dialyzate exchanges were collected and analyzed for silicon content by ICP–AES, as most soluble species are removed during the first exchanges when the

concentration gradient with the dialyzate is the largest. Dialysis procedures were carried out for four days, during which the pH of the colloid solutions reached approximately that of the dialyzates. Stöber silica nanoparticles synthesized with an ammonia catalyst instead of L-arginine were also dialyzed for comparison purposes. The ICP–AES results are summarized in Table 1. With the arginine-synthesized 37 and 138 nm diameter silica colloids dialyzed against pure water, the Si content decreased to near or below the detection limit (0.01 ppm) by the third exchange, signaling that the dialysis was already nearing completion at this stage. However, when the same colloids were dialyzed against L-arginine, the amount of Si detected in the dialyzate was higher and was still elevated by the third solvent exchange. This increased loss of Si species can be attributed to the excess L-arginine etching of the arginine-stabilized silica nanoparticles, accelerated by stirring and separated by dialysis, which continuously drive the silica solubility equilibrium toward dissolution. Blank sample analyses indicated only trace amounts of detectable silicon species from the containers, so the results may be confidently attributed to the reactivity of the colloidal sols.

In comparison with the arginine-derived silicas, the 65 nm diameter Stöber silica colloids released larger amounts of silicon-containing species when dialyzed against water, but lower amounts when dialyzed against the arginine buffer. However, when comparing Si loss between different size colloids, one must also consider the total amount of silica in each sample. Dialyses were conducted at a constant volume ratio (10 mL colloidal sol/1000 mL dialyzate), but solutions of different size colloids contained different amounts of silica. The silica concentration (determined by weighing dried residues from evaporated sols) was 7.3 mg/mL for 37 nm, 18.2 mg/mL for 138 nm, and 39.0 mg/mL for 65 nm colloids. The loss of Si during dialysis against arginine buffer, relative to the original silica concentration, was similar for the two arginine-synthesized colloids (3.49 ppm for 37 nm vs 3.37 ppm for 138 ppm when scaled by the 37 nm/138 nm concentration ratio), but was lower for Stöber silica (0.61 ppm when scaled as a ratio of the 37 nm/65 nm concentrations). This indicates that the L-arginine-derived silica dissolved to a greater extent in the presence of arginine in comparison to the ammonia-derived silica.

The addition of L-arginine to the dialyzate raises the pH of the solution, which increases the rate of dissolution of amorphous silica nanoparticles. Studies of the dissolution of silica colloids in different media have shown that their solubility depends on particle size (smaller particles are more soluble) and the synthetic method (which affects the hydroxyl content).^{36–40} The pH of L-arginine dialyzates for 37 and 138 nm silica (Table 2) was indeed higher than that of the colloid solutions prior to dialysis, although the pH increase was small

Table 2. pH Colloidal Solutions and Dialyzate Solutions

solution	pH
water	6.16 ± 0.02
nonpurified 37 nm colloidal solution	8.50 ± 0.01
3.3 mM L-arginine dialyzate (for 37 nm silica dialysis)	9.31 ± 0.01
nonpurified 138 nm colloidal solution	9.21 ± 0.01
4.5 mM L-arginine dialyzate (for 138 nm silica dialysis)	9.55 ± 0.01
nonpurified 65 nm Stöber silica solution	10.70 ± 0.02
4.5 mM L-arginine dialyzate (for 65 nm silica dialysis)	9.24 ± 0.01

(0.19 units) for 138 nm silica. The pH of the 65 nm Stöber silica was more basic (10.70) because of the ammonia catalyst and decreased upon dialysis against water or L-arginine.

TEM images in Figure 3 corroborated the ICP–AES analysis results, in which the diameters of the 37.2 ± 3.0 and

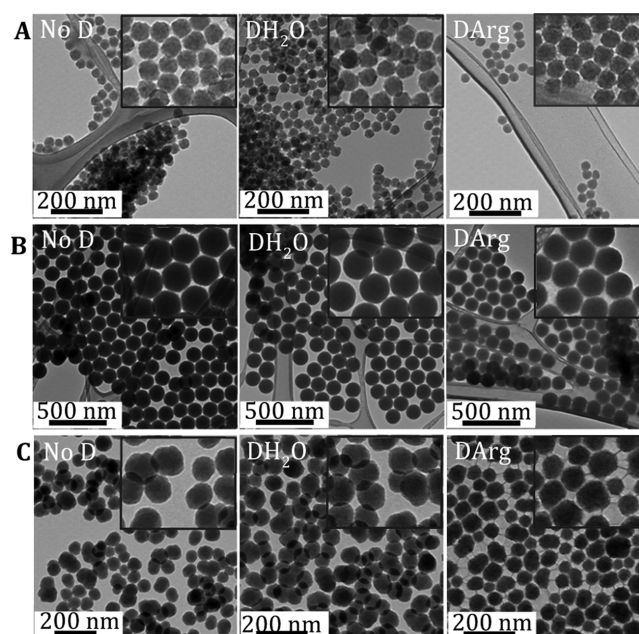


Figure 3. Series (a) images are 37 nm L-arginine-synthesized silica, series (b) images are 138 nm L-arginine-synthesized silica nanoparticles, and series (c) images are 65 nm ammonia-synthesized silica. Insets of each image series are on equal scale with each other for direct comparison. No D = no dialysis/as-prepared, DArg = dialyzed against L-arginine solution, and DH₂O = dialyzed against pure water.

137.9 ± 5.7 nm silica spheres decreased to 33.7 ± 3.1 and 119.1 ± 8.9 , respectively, after dialysis in L-arginine. Less dissolution occurred with water dialysis, which resulted in average diameters of 35.7 ± 2.5 and 135.9 ± 5.9 nm, respectively. The nanoparticles did not show any visible evidence of interior hollowing with dissolution. The size of the 65.3 ± 8.6 nm Stöber silica colloid (ammonia-based preparation) remained constant after water dialysis (65.4 ± 10.5 nm), but decreased slightly after dialysis in L-arginine, with a concomitant increase in polydispersity (60.0 ± 13.0 nm) and subtle changes in colloid shape.

In Figure 3a,b, the L-arginine-treated particles are increasingly faceted and appear to be encapsulated in a halo of less dense material than the core. The effect of L-arginine on the packing behavior is most noticeable with the 138 nm silica colloids because of their smoother, rounder morphology (Figure 3b). The unmodified 138 nm silica particles ordered into two-dimensional (2D) hexagonal arrays upon drying on the TEM grid, and the particles were slightly faceted at their contacting surfaces. After water dialysis, the particles still ordered, but they maintained their rounded shape. Upon dialysis against L-arginine, the 138 nm silica ordered with distinct faceting at interparticle boundaries. The 37 nm silica behaved similarly, but the faceting was less pronounced, possibly because of the smaller particle size and the inherent surface roughness already present prior to dialysis.

The evidence of increased dissolution in the presence of added L-arginine, in combination with the observed assembly

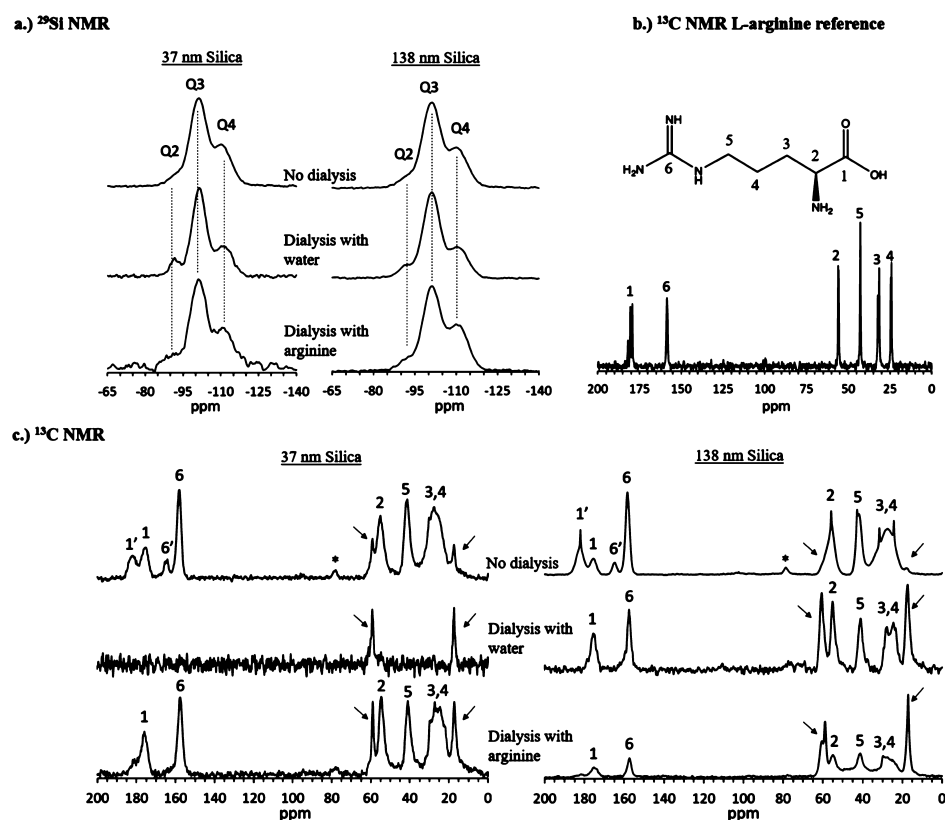


Figure 4. (a) ^{29}Si NMR spectra of 37 nm (left) and 138 nm (right) silica nanoparticles, (b) ^{13}C CP-MAS NMR reference spectrum of L-arginine powder as received, and (c) ^{13}C CP-MAS NMR series for 37 nm (left) and 138 nm silica nanoparticles (right). All nanoparticles were synthesized using L-arginine. Numbers match peaks from the L-arginine reference spectrum in (e). Arrows indicate ethoxy peaks from incompletely hydrolyzed TEOS or surface silica groups that have condensed with ethanol. Asterisks denote spinning side bands.

of colloids into 2D arrays, makes for a reasonable argument that L-arginine may facilitate particle deformation through a surface hydrolysis mechanism. NMR data (see below) are consistent with this idea. The 65 nm colloids made by the Stöber method (Figure 3c) are polydisperse, but exhibited an interesting packing behavior in the presence of L-arginine. The packing of these particles was disordered in the undialyzed and water-dialyzed samples, but the arginine-dialyzed particles formed monolayers with contacting facets, deformed interfaces, and minimal particle–particle overlap. Additionally, the particles appeared bridged together by a web of thin filaments. The bridges appear to be siliceous because some of them persist even after calcination at 600 °C. This webbing/bridging phenomenon is not completely understood, but may develop from arginine and silica residues that form filaments during drying. These structures were observed to some extent in TEM images of all the silica samples (least of which in water-dialyzed samples).

NMR Spectroscopy. Solid-state ^{13}C and ^{29}Si CP-MAS NMR studies were performed on the as-prepared, dialyzed with water, and dialyzed with L-arginine solution colloids in order to gain further insight into the chemical changes that occurred during dialysis. Detailed peak positions for the 37 and 138 nm silica colloids are tabulated in Table S1, and the spectra are shown in Figure 4. The CP-MAS data are not strictly quantitative, so the data are interpreted qualitatively. The ^{29}Si NMR spectra of the as-prepared 37 and 138 nm silica colloids are similar and indicate that a majority of Si atoms are present in singly hydroxylated Q^3 sites, followed by Q^4 (bulk silica), and finally doubly hydroxylated Q^2 groups. After

dialysis against water, the hydroxylated content increased slightly for both colloid sizes. This aligns with our expectations because at this lower pH, a greater proportion of silica surface groups are protonated (as silanols) and free of electrostatically associated arginine. In the L-arginine-dialyzed samples, the intensity of the Q^2 and Q^3 peaks diminished and that of the Q^4 peaks increased. This suggests silica dissolution in basic L-arginine solution, where the near-surface hydroxylated silica groups react first.

^{13}C spectra of the colloids and an L-arginine powder reference spectrum are also shown in Figure 4. Table S2 details peak positions and Table S3 summarizes the deconvoluted ^{29}Si peak areas. The L-arginine peaks are prominent in all samples (peaks numbers 1 through 6) except the water-dialyzed 37 nm silica nanoparticles. For this sample, only the two ethoxy peaks remain weakly discernible above the baseline noise (indicated by arrows in all spectra in Figure 4). The ethoxy peaks have been noted in other studies and are thought to be either underreacted TEOS or ethoxy-terminated groups from silanols that exchanged their hydroxyls with ethanol during synthesis.³¹ The arginine peaks are shifted slightly upfield in the silica samples compared to pure L-arginine powder, which may reflect their charge state from electrostatic association with the nanoparticles. Dialysis with L-arginine resulted in additional peak splitting (peaks 1' and 6'), especially at carbons 1 and 6 because of polymorphism. The 138 nm silica particles did not release all of the L-arginine during dialysis in water. This is supported by previous literature reports, where even longer and more extensive dialyses could not completely remove L-arginine from silica. This implies that a portion of the L-

arginine is encapsulated during regrowth synthesis and cannot diffuse out of larger nanoparticles during dialysis.^{31,38} Dialysis against L-arginine solution substantially lowered the intensity of the silica ethoxy peaks in both the 37 and 138 nm samples. This can be attributed to increased hydrolysis and dissolution due to the added L-arginine.

NMR spectra for the Stöber-type 65 nm silica colloids (Figure S2), like the 37 and 138 nm silica, show less intense ethoxy peaks following dialysis. Dialysis against L-arginine solution gave ¹³C spectra with additional weak, broad peaks aligned with L-arginine residues. The ²⁹Si NMR spectra were also similar to the L-arginine-synthesized silica, but with a complete loss of Q² geminal hydroxyls after L-arginine dialysis. The basic conclusions were the same for all three colloids, namely, that water dialysis increased the intensity of Q² and/or Q³ peaks and L-arginine dialysis diminished their intensity. In contrast, the 138 nm arginine-prepared silica retained some L-arginine content (which was presumably incorporated during synthesis) after dialysis and the peaks attributed to ethoxy groups decreased in intensity but did not disappear entirely. The retention of L-arginine and undercondensed silica components in the interior of the particles suggests that L-arginine–silica, especially the larger 138 nm colloids, is less condensed and more susceptible to chemical dissolution and ripening than Stöber-type silica.

Effect of L-Arginine Addition on Colloidal Crystal Film Assembly. L-Arginine (2.9 mM) was added to the as-prepared and dialyzed colloidal solutions to determine its effects under colloidal assembly conditions (slow vertical evaporation) and for comparison with the original observations (examples in Figures 1 and 2). The TEM images in Figure 3 imply a correlation between colloid shape deformation/interparticle bridge reactions and dissolution involving L-arginine. All colloidal solutions used in this set of experiments were the 138 nm L-arginine-prepared silica (all colloidal sols 10 times diluted with water). Colloidal films were deposited at 40 °C (~85% humidity). Representative images of the 138 nm sample series are included in Figure 5 to highlight typical results. The results presented were based primarily on top-surface SEM images collected from start to end of the 1 to 1.5 × 1 cm films. The number of images collected per film depended on the structural complexity of the film and could number >50 images. Some of the samples discussed below required only a few images as they were disordered or were covered in large amounts of organic/silica residues. Cross-sectional images were also collected and yielded corroborating results (such as interparticle bridging, shape deformation, etc.) to the top surface (see, e.g., Figure 5f).

Nondialyzed silica showed regions of spherical particles with interspersed regions of hexagonally faceted particles as shown in Figure 5a. Deformation qualitatively correlated with the tightness and symmetry of particle packing arrangements and thin bridge growths were observed between nearest silica particle neighbors. Although the bridges could not be observed in the tightest packing situations, they may still be present. These bridges are visible with close observation in Figure 5a. With the addition of L-arginine (Figure 5b), the assembled silica had a coated appearance with wider regions of faceting. Interparticle bridge projections were more frequent, examples of which are shown in the inset of Figure 5b. The size of the nanoparticles did not noticeably decrease with the L-arginine addition, unlike those dialyzed against an L-arginine solution. This is likely because of the concentration gradient in dialysis

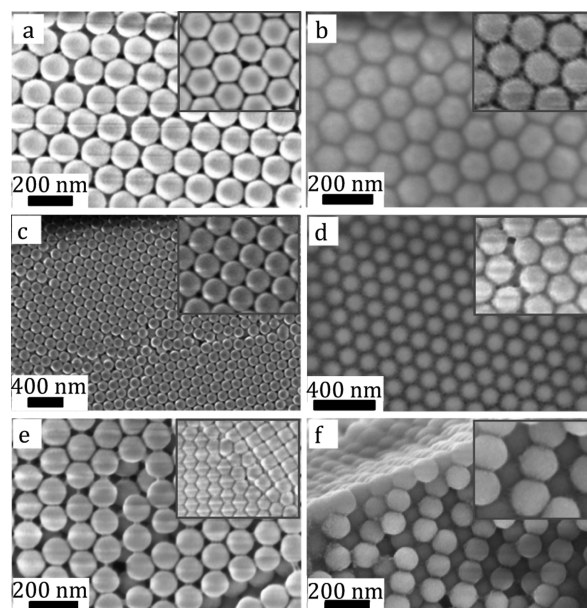


Figure 5. Silica colloidal films (138 nm) evaporated (40 °C) with and without arginine (2.9 mM) added to the depositing solutions. Nondialyzed silica without (a) and with (b) L-arginine added, water-dialyzed silica without (c) and with (d) arginine added, and arginine-dialyzed silica without (e) and with (f) arginine added (cross-sectional view).

that accelerates the reaction by removing dissolved silicate species.

Water-dialyzed particles (Figure 5c) retained their spherical shape with noticeably fewer interparticle bridges and shorter-range ordering because of weaker colloid repulsion at lower pH. In some areas, silica nanoparticles were observed to coalesce. With the addition of L-arginine in Figure 5d, frequent interparticle bridging occurred (noticeable in the inset of Figure 5d) and the nanoparticles packed more tightly, faceting as shown in the inset view in Figure 5d.

In Figure 5e, a film was deposited from an arginine-dialyzed 138 nm silica solution. Patchy portions of the film still contained spherical particles, but a majority of the film featured tightly packed, faceted nanoparticles and prominent bridging wherever interparticle spaces could be visualized. There was significant secondary nanoparticle growth at the leading edge of the film, but it stopped after the first few microns of film growth. This could be because of continuous silica dissolution during dialysis (a source of reactive soluble silicates) in conjunction with the higher pH (higher arginine concentration), conditions that favor nucleation of new particle seeds. The addition of more arginine to these colloids, followed by evaporative film deposition, resulted in films with noticeably coated colloids as seen in Figure 5f (cross-sectional view). The inset of Figure 5f also reveals new faceting growth that formed during assembly, sculpting vertices (Figure 3). Similar to Figure 5e, particles packed or bridged to fill all spaces and wherever the spacing could be visualized.

It should be noted that some degree of nonuniformity was observed in most samples. For example, in Figure 5e, there was widespread secondary nanoparticle growth at the start of the film, but it was scarce to nonexistent throughout the rest of the film. Several factors can contribute to nonuniform film packing, such as film edge and grain boundary effects, as well as demixing of film components during the static evaporation

process. Thus, TEOS and other precursors may not be uniformly distributed at all stages of film growth.

The interparticle bridging and shape changes noted all appear to have siliceous origins. A collection of images of sintered colloidal films (700 °C in air) is shown in Figure S4. The shape changes persist (with some shrinkage) after heating to temperatures where the organic components are completely removed.

These results, in combination with the NMR data, illustrate the complex and opportunistic role of L-arginine in reshaping silica nanoparticle suspensions. L-Arginine facilitates heterogeneous reactions between the assembling solid colloidal crystal and solution, as best evidenced by the appearance and frequency of interparticle bridge formation. The colloids assembled as expected for hard spheres when free L-arginine was removed by dialysis (Figure 5c). However, with L-arginine present, the colloids can deform in order to pack more tightly and close interparticle voids. The shape changes appear to depend on the arginine concentration, which may be because of silica solubility or the ability of the silica to encapsulate and release arginine.

For comparison purposes, assembly experiments were run at a higher temperature, closer to the arginine-catalyzed silica synthesis conditions, 60 °C (~5% humidity), and gave similar results. Silica of 37 nm was studied in parallel, and images summarizing these results are shown in Figure S5. The 37 nm films responded similarly (to 138 nm silica) to arginine addition, but did not display changes that were as striking as the 138 nm particles. This was partly because of the lower image resolution of smaller particles, as well as to their faceted morphology prior to any treatment.

Effect of TEOS Addition on the Colloidal Crystal Film Assembly. We also tested the effect of adding the silica precursor during colloidal crystal evaporative deposition, which introduced an additional source of silica that could promote shape ripening, silica regrowth, or new nanoparticle nucleation reactions. TEOS (tetraethyl orthosilicate) was mixed in with 5 mL of colloidal solutions (0, 4.5, 9, and 45 mM TEOS) immediately before starting the evaporative deposition. We also tested combined additions of 4.5 mM TEOS with 2.9 mM L-arginine in the 5 mL of colloid solutions. Experiments were again conducted at 40 °C/80–85% humidity. Selected images summarizing results are shown in Figure 6.

TEOS addition to nondialyzed 138 nm silica nanoparticle dispersions (Figure 6a,b) resulted in thickened/increased interparticle bridging. New nanoparticle formation and regions of colloidal surface coating/texturing were noted (Figure 6b), especially at the leading edge of the films. These effects increased with increasing amounts of TEOS or if additional arginine (catalyst) was added with TEOS.

Water-dialyzed silica colloids maintained approximately spherical shapes and did not form elaborate networks of interparticle bridging with TEOS addition. Instead, the colloids sometimes formed short fusion-type contacts in close packing situations (Figure 6c). This was likely because of the removal of underreacted silicates and free L-arginine residues during dialysis, rendering the particle surfaces and solution less reactive. In the absence of the basic catalyst, TEOS addition alone did not trigger significant new nanoparticle growth. However, adding a combination of arginine and TEOS generated some new nanoparticle growth, a dramatic increase in interparticle bridging (inset of Figure 6d), and nonspherical shape deformations (Figure 6d).

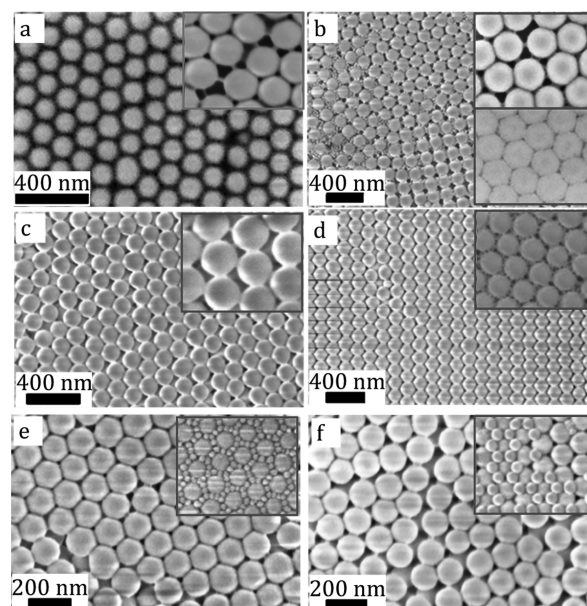


Figure 6. SEM images of 138 nm silica treated with TEOS or TEOS + arginine. (a) Nondialyzed with 2.9 mM L-arginine + 4.5 mM TEOS, (b) nondialyzed with 4.5 mM TEOS, (c) water-dialyzed with 2.9 mM L-arginine + 4.5 mM TEOS, (d) water-dialyzed with 4.5 mM TEOS, (e) L-arginine-dialyzed with 9 mM TEOS, and (f) L-arginine-dialyzed with 2.9 mM L-arginine + 4.5 mM TEOS.

Conversely, L-arginine-dialyzed 138 nm silica exhibited thickened interparticle bridge projections and abundant secondary nanoparticle nucleation and growth with TEOS addition (Figure 6e,f) because of the higher concentration of the arginine catalyst. Some colloid surface texturing/edge growth could be seen at higher resolution. Nonspherical shape deformation was common, but this behavior was already present in the arginine-dialyzed silica prior to TEOS addition (Figure 5e,f). Larger additions of TEOS or TEOS + arginine resulted in the growth of larger and more numerous new nanoparticles.

In summary, the addition of TEOS provided silica precursor material for bridging-type reactions between assembling particles and new nanoparticle nucleation and growth (when arginine was present), as well as for colloidal surface texturing. The nanoparticle diameters did not appreciably change with TEOS addition. This aligns with expectations, as aged silica colloids (>1–2 days old) tend to resist regrowth. TEOS did not drive bulk colloid shape deformations, but may be involved in some surface shaping as evidenced by bridge formation and surface texturing/faceting. Deposition at a higher temperature (60 °C) drove more of these effects, especially new nanoparticle growth. Parallel experiments conducted with 37 nm silica yielded similar results (Figure S6). Blank samples run without colloids present (not shown) produced bulk silica and polydisperse nano- or microspheres with TEOS or TEOS + L-arginine solutions.

Binary Colloidal Crystal Films. Dialyzed and nondialyzed binary mixtures of two colloids (138 and 37 nm in a 4:1 volume ratio) were deposited and are compared in Figures 7–9. The addition of L-arginine and TEOS as in the previous sections was also studied. Figure 7 shows nondialyzed binary mixtures, Figure 8 is water-dialyzed, and Figure 9 is arginine-dialyzed. Films were grown without any additives in the

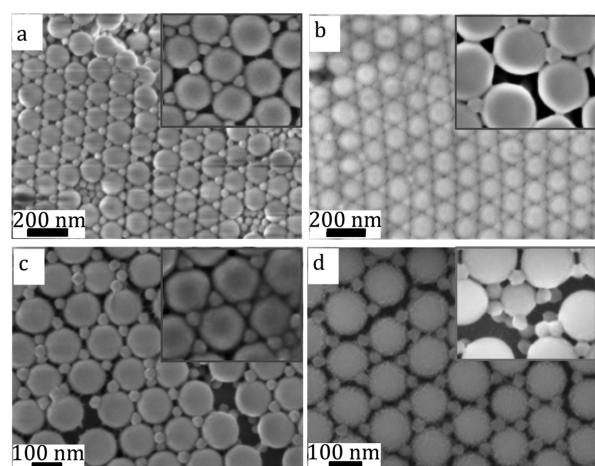


Figure 7. SEM micrographs of binary films of nondialyzed 138 and 37 nm silica particles (4:1 by volume ratio) deposited onto silicon substrates by the vertical evaporation method with (a) no additives, (b) 4.5 mM TEOS (9 mM in the inset) added, (c) 2.9 mM L-arginine added, and (d) TEOS (4.5 mM) + L-arginine (2.9 mM) added.

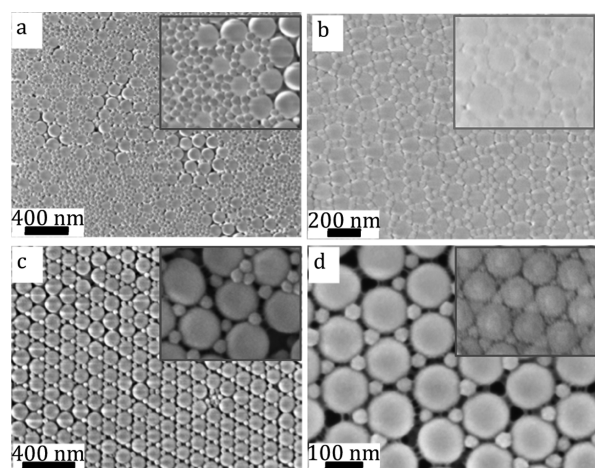


Figure 8. SEM micrographs of binary films of water-dialyzed 138 and 37 nm silica (4:1 by volume ratio) deposited onto silicon substrates by the vertical evaporation method with (a) no additives, (b) 4.5 mM TEOS (9 mM in the lower inset) added, (c) 2.9 mM L-arginine added, and (d) TEOS (4.5 mM) + L-arginine (2.9 mM) added.

depositing solution (a), with TEOS added (b), with L-arginine added (c), and with TEOS + arginine added (d).

The results shown in Figure 7 for nondialyzed colloids align with the above observations (Figures 5 and 6) in which arginine was already present from the synthesis. Shape deformation and interparticle bridging are evident without the addition of TEOS or extra arginine (Figure 7a). Adding TEOS (Figure 7b) increased colloidal surface texturing/faceting and thickened interparticle bridges between neighboring nanoparticles. The “fuzzy” surface texturing in Figure 7b matches the textural changes noted in Figure 1e (nondialyzed silica) as well as in the lower inset of Figure 6b (TEOS + arginine added to nondialyzed 138 nm silica). The interparticle bridging on the 37 nm silica occurred at vertices and along facets connected to the larger 138 nm silica particles, accentuating their shapes (insets of Figure 7b,d), similar to that seen in Figure 1f,g. In Figure 7c, both sizes of silica nanoparticles appeared to deform more when treated with excess arginine only. In Figure 7d, adding a combination of

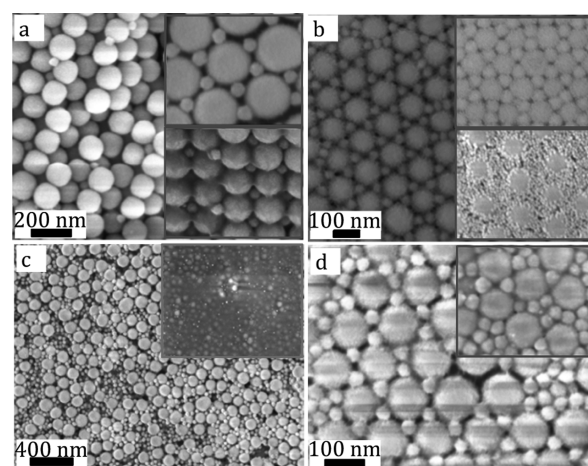


Figure 9. SEM micrographs of binary films of water-dialyzed 138 and 37 nm silica (4:1 by volume ratio) deposited onto silicon substrates by the vertical evaporation method with (a) no additives (cross-sectional view), (b) 4.5 mM TEOS added at 40 °C, (c) 2.9 mM L-arginine added, and (d) TEOS (4.5 mM) + L-arginine (2.9 mM) added.

TEOS and arginine resulted in excess coating over the film and some small new nanoparticle growth. The inset of Figure 7d shows a clearer example of the extended borders of the 37 nm silica particles, forming facets that increase contact with their 138 nm neighbors, much like that observed in Figure 1f. New nanoparticle growth was not as pervasive in these samples as in the single-sized dispersions (Figures 5 and 6), which could be because of the higher particle densities in binary mixtures. Higher particle density provides more surface area for heterogeneous reactions between the solution and the solid, so growth competes more effectively with nucleation.

The preferred binary phase is an AB₂-type structure as seen in Figure 7. However, the primary packing arrangement was notably different in the water-dialyzed sample with the removal of free arginine (Figure 8a). The packing geometry did not recover with TEOS addition alone (Figure 8b), but recovered once arginine was reintroduced into the solution (Figure 8c,d). The phase behavior of binary silica colloidal crystals is complex, but a correlation between the phase behavior and amino acid content has also been noted in earlier work.³⁴ The water-dialyzed samples in Figure 8 showed little interparticle bridging/shape deformation (Figure 8a) until arginine was reintroduced (Figure 8c,d). TEOS addition, with or without added arginine, again induced some texturing changes on the nanoparticle surfaces (insets of Figure 8b,d). A cross-sectional image (Figure S7) illustrates the texture that results in TEOS addition. There appears to be a very thin overgrowth on the top surface of the film.

Finally, the arginine-dialyzed samples in Figure 9 show a dramatic increase in surface texturing, interparticle bridging, and secondary nanoparticle growth. This effect is subtler in films grown with no additives (Figure 9a) and is evident when TEOS is added to the colloidal solution (Figure 9b). Adding even more arginine (Figure 9c) disrupted the ordering significantly and formed regions that contained large amounts of organic residues (inset). The addition of L-arginine combined with TEOS (Figure 9d) resulted in larger new nanoparticle growth and surface texturing/coating. Non-spherical particle deformations were present in every sample.

Based on these results, we can conclude that the addition of L-arginine and TEOS amplifies the unusual interparticle bridging and morphological changes that we observe with colloidal crystals grown from nondialyzed colloids (Figures 1 and 2). Images of films grown with TEOS added (Figures 6b, 7b, 8b,d, and 9b,d) show thickened bridges and surface texturing or shell growth, indicating that surface reactions can occur between the colloids and incompletely reacted silicates during the course of evaporative assembly. These effects are accelerated by the presence of arginine, but noticeably diminish with water dialysis and the removal of trace soluble silicates and arginine.

CONCLUSIONS

In the evaporative assembly of nondialyzed L-arginine-stabilized silica nanoparticles, particle shape changes and interparticle bridges form within the newly deposited colloidal crystals. The shape changes and bridging depend on the local packing geometry and can be rationalized as a ripening process that lowers the free energy of the colloidal crystal through higher interconnectivity and packing density. L-Arginine facilitates shape ripening, bridge formation, and under some conditions, the nucleation of new silica nanoparticles during evaporative colloidal assembly.

ssNMR data indicate that the arginine-capped silica particles encapsulate a significant amount of arginine and incompletely condensed silica, much of which can be leached out by dialysis. The encapsulated L-arginine increases the solubility and dissolution rate because it buffers the solution at a basic pH, affecting the hydrolysis/olation equilibrium of silica. During dialysis with arginine, we observed accelerated silica degradation and hydrolysis by ICP–AES as well as shifts in the hydroxyl composition in ssNMR. This “softening” effect facilitates the particle deformation observed with increasing amounts of L-arginine in the depositing solutions. Conversely, nanoparticles dialyzed against pure water were less susceptible to shape changes because of the removal of L-arginine and soluble silicates. Stöber silica particles (synthesized with ammonia instead of arginine) underwent shape changes and interparticle bridging only upon introduction of L-arginine during dialysis (Figure 3c), again highlighting the role of L-arginine in the shape changes of silica colloids that were observed in the dried films.

By adding L-arginine and/or TEOS to the depositing colloidal solutions, we were able to further drive the unusual morphological changes seen in colloidal crystal films deposited under ordinary conditions. Shape ripening and bridge formation involve heterogeneous reactions that require the presence of the solid colloidal crystal framework. TEOS addition provided a source of silica for these reactions as evidenced by thickening bridges and building up of facets, but could also cause supersaturation and the nucleation of new particles in solution when added in higher concentrations in the presence of excess L-arginine. TEOS addition did not significantly affect the size of the silica colloids as it favored nucleation instead of growth, as expected in the basic L-arginine environment. This resulted in the formation of mixed colloid films and binary colloidal crystals as shown in Figure 6e.

The growth of ordered assemblies of nonspherical nanoparticles is of interest for fundamental studies and applications involving shape-dependent physical and electronic properties of both colloidal crystals and replica structures. We have shown

here that controlling the solution environment and particle packing geometry can drive faceting and bridging in silica colloidal crystals. Under the conditions of our experiments, polycrystalline colloidal crystal films were typically obtained and it was difficult to produce a single colloid shape or type of deformation over long lateral distances. There is a possibility of achieving better control over the assembly process and perhaps achieving more interesting symmetry breaking by combining shape-ripening chemistry with other assembly techniques, for example, using mechanical tension and compression at a liquid interface as in the Langmuir–Blodgett technique. These possibilities and the properties of replica structures will be explored in future experiments.

ASSOCIATED CONTENT

Supporting Information

The Supporting Information is available free of charge on the ACS Publications website at DOI: 10.1021/acsami.8b17907.

SEM images of 37 and 138 nm silica nanoparticles and ssNMR data (PDF)

AUTHOR INFORMATION

Corresponding Author

*E-mail: tem5@psu.edu.

ORCID

Thomas E. Mallouk: 0000-0003-4599-4208

Notes

The authors declare no competing financial interest.

ACKNOWLEDGMENTS

This work was supported by the National Science Foundation under MRSEC grant number DMR-1420620. We thank Carlos Pacheco for assistance with obtaining and interpreting NMR data and Laura Jean Liermann for assistance with ICP–AES measurements and data analysis.

ABBREVIATIONS

ICP–AES, inductively coupled plasma atomic emission spectroscopy
TEM, transmission electron microscopy
SEM, scanning electron microscopy
ssNMR, solid-state nuclear magnetic resonance spectroscopy

REFERENCES

- (1) Zhang, H.; Liu, M.; Zhou, F.; Liu, D.; Liu, G.; Duan, G.; Cai, W.; Li, Y. Physical deposition improved SERS stability of morphology controlled periodic micro/nanostructured arrays based on colloidal templates. *Small* **2014**, *11*, 844–853.
- (2) Ge, J.; Yin, Y. Magnetically responsive colloidal photonic crystals. *J. Mater. Chem.* **2008**, *18*, 5041–5045.
- (3) Malepourkoupaei, A.; Kostiuik, L. W.; Harrison, D. J. Fabrication of binary opal lattices in microfluidic devices. *Chem. Mater.* **2013**, *25*, 3808–3815.
- (4) Liu, J.; Cai, Y.; Deng, Y.; Sun, Z.; Gu, D.; Tu, B.; Zhao, D. Magnetic 3-D ordered macroporous silica templated from binary colloidal crystals and its application for effective removal of microcystin. *Microporous Mesoporous Mater.* **2010**, *130*, 26–31.
- (5) Talapin, D. V.; Shevchenko, E. V.; Bodnarchuk, M. I.; Ye, X.; Chen, J.; Murray, C. B. Quasicrystalline order in self-assembled binary nanoparticle superlattices. *Nature* **2009**, *461*, 964–967.
- (6) Wang, J.; Ahl, S.; Li, Q.; Kreiter, M.; Neumann, T.; Burkert, K.; Knoll, W.; Jonas, U. Structural and optical characterization of 3D

binary colloidal crystal and inverse opal films prepared by direct co-deposition. *J. Mater. Chem.* **2008**, *18*, 981–988.

(7) Phillips, K. R.; England, G. T.; Sunny, S.; Shirman, E.; Shirman, T.; Vogel, N.; Aizenberg, J. A colloidoscope of colloid-based porous materials and their uses. *Chem. Soc. Rev.* **2016**, *45*, 281–322.

(8) Burke, K. A.; Brenckle, M. A.; Kaplan, D. L.; Omenetto, F. G. Evaluation of the spectral response of functionalized silk inverse opals as colorimetric immunosensors. *ACS Appl. Mater. Interfaces* **2016**, *8*, 16218–16226.

(9) Stein, A.; Schroden, R. C. Colloidal crystal templating of three-dimensionally ordered macroporous solids: materials for photonics and beyond. *Curr. Opin. Solid State Mater. Sci.* **2001**, *5*, 553–564.

(10) Wijnhoven, J. E.; Vos, W. L. Preparation of photonic crystals made of air spheres in titania. *Science* **1998**, *281*, 802–804.

(11) Boppella, R.; Kochuveedu, S. T.; Kim, H.; Jeong, M. J.; Marques Mota, F.; Park, J. H.; Kim, D. H. Plasmon-Sensitized Graphene/TiO₂ Inverse Opal Nanostructures with Enhanced Charge Collection Efficiency for Water Splitting. *ACS Appl. Mater. Interfaces* **2017**, *9*, 7075–7083.

(12) Pérez-Page, M.; Yu, E.; Li, J.; Rahman, M.; Dryden, D. M.; Vidu, R.; Stroeve, P. Template-based syntheses for shape controlled nanostructures. *Adv. Colloid Interface Sci.* **2016**, *234*, 51–79.

(13) Glotzer, S. C.; Solomon, M. J. Anisotropy of building blocks and their assembly into complex structures. *Nat. Mater.* **2007**, *6*, 557–562.

(14) van Dillen, T.; van Blaaderen, A.; Polman, A. Shaping colloidal assemblies. *Mater. Today* **2004**, *7*, 40–46.

(15) Chen, C.; Wylie, R. A. L.; Klinger, D.; Connal, L. A. Shape control of soft nanoparticles and their assemblies. *Chem. Mater.* **2017**, *29*, 1918–1945.

(16) Velikov, K. P.; van Dillen, T.; Polman, A.; van Blaaderen, A. Photonic crystals of shape-anisotropic colloidal particles. *Appl. Phys. Lett.* **2002**, *81*, 838–840.

(17) Phillips, K. R.; Vogel, N.; Hu, Y.; Kolle, M.; Perry, C. C.; Aizenberg, J. Tunable anisotropy in inverse opals and emerging optical properties. *Chem. Mater.* **2014**, *26*, 1622–1628.

(18) Ye, X.; Chen, J.; Engel, M.; Millan, J. A.; Li, W.; Qi, L.; Xing, G.; Collins, J. E.; Kagan, C. R.; Li, J.; Glotzer, S. C.; Murray, C. B. Competition of shape and interaction patchiness for self-assembling nanoplates. *Nat. Chem.* **2013**, *5*, 466–473.

(19) Míguez, H.; Meseguer, F.; López, C.; Blanco, Á.; Moya, J. S.; Requena, J.; Mifsud, A.; Fornés, V. Control of the Photonic Crystal Properties of fcc-Packed Submicrometer SiO₂ Spheres by Sintering. *Adv. Mater.* **1999**, *10*, 480–483.

(20) Wang, Y.; Wang, Y.; Zheng, X.; Yi, G.-R.; Sacanna, S.; Pine, D. J.; Weck, M. Three-dimensional lock and key colloids. *J. Am. Chem. Soc.* **2014**, *136*, 6866–6869.

(21) Routh, A. F.; Russel, W. B. Deformation mechanisms during latex film formation: experimental evidence. *Ind. Eng. Chem. Res.* **2001**, *40*, 4302–4308.

(22) Tirumkudulu, M. S.; Russel, W. B. Role of capillary stresses in film formation. *Langmuir* **2004**, *20*, 2947–2961.

(23) Keddie, J. L.; Meredith, P.; Jones, R. A. L.; Donald, A. M. Kinetics of Film Formation in Acrylic Latices Studied with Multiple-Angle-of-Incidence Ellipsometry and Environmental SEM. *Macromolecules* **1995**, *28*, 2673–2682.

(24) Dobler, F.; Pith, T.; Lambla, M.; Holl, Y. Coalescence mechanisms of polymer colloids. *J. Colloid Interface Sci.* **1992**, *152*, 1–11.

(25) Dobler, F.; Pith, T.; Lambla, M.; Holl, Y. Coalescence mechanisms of polymer colloids. *J. Colloid Interface Sci.* **1992**, *152*, 12–21.

(26) Hartlen, K. D.; Athanasopoulos, A. P. T.; Kitaev, V. Facile Preparation of Highly Monodisperse Small Silica Spheres (15 to >200 nm) Suitable for Colloidal Templating and Formation of Ordered Arrays. *Langmuir* **2008**, *24*, 1714–1720.

(27) Watanabe, R.; Yokoi, T.; Kobayashi, E.; Otsuka, Y.; Shimojima, A.; Okubo, T.; Tatsumi, T. Extension of size of monodisperse silica

nanospheres and their well-ordered assembly. *J. Colloid Interface Sci.* **2011**, *360*, 1–7.

(28) Stöber, W.; Fink, A.; Bohn, E. Controlled growth of monodisperse silica spheres in the micron size range. *J. Colloid Interface Sci.* **1968**, *26*, 62–69.

(29) Jiang, P.; Bertone, J. F.; Hwang, K. S.; Colvin, V. L. Single-crystal colloidal multilayers of controlled thickness. *Chem. Mater.* **1999**, *11*, 2132–2140.

(30) Russell, J. L.; Noel, G. H.; Warren, J. M.; Tran, N.-L. L.; Mallouk, T. E. Binary colloidal crystal films grown by vertical evaporation of silica nanoparticle suspensions. *Langmuir* **2017**, *33*, 10366–10373.

(31) Akbey, Ü.; Altin, B.; Linden, A.; Özçelik, S.; Gradzielski, M.; Oschkinat, H. Dynamic nuclear polarization of spherical nanoparticles. *Phys. Chem. Chem. Phys.* **2013**, *15*, 20706–20716.

(32) Yokoi, T.; Wakabayashi, J.; Otsuka, Y.; Fan, W.; Iwama, M.; Watanabe, R.; Aramaki, K.; Shimojima, A.; Tatsumi, T.; Okubo, T. Mechanism of formation of uniform-sized silica nanospheres catalyzed by basic amino acids. *Chem. Mater.* **2009**, *21*, 3719–3729.

(33) Fouilloux, S.; Taché, O.; Spalla, O.; Thill, A. Nucleation of silica nanoparticles measured in situ during controlled supersaturation increase. Restructuring toward a monodisperse nonspherical shape. *Langmuir* **2011**, *27*, 12304–12311.

(34) Kung, S.-C.; Chang, C.-C.; Fan, W.; Snyder, M. A. Template-free ordered mesoporous silicas by binary nanoparticle assembly. *Langmuir* **2014**, *30*, 11802–11811.

(35) Bruna, M.; Chapman, S. J. Excluded-volume effects in the diffusion of hard spheres. *Phys. Rev. E: Stat., Nonlinear, Soft Matter Phys.* **2012**, *85*, 011103.

(36) Alexander, G. B.; Heston, W. M.; Iler, R. K. The solubility of amorphous silica in water. *J. Phys. Chem.* **1954**, *58*, 453–455.

(37) Alexander, G. B. The effect of particle size on the solubility of amorphous silica in water. *J. Phys. Chem.* **1957**, *61*, 1563–1564.

(38) Yamada, H.; Urata, C.; Aoyama, Y.; Osada, S.; Yamauchi, Y.; Kuroda, K. Preparation of colloidal mesoporous silica nanoparticles with different diameters and their unique degradation behavior in static aqueous systems. *Chem. Mater.* **2012**, *24*, 1462–1471.

(39) Rimer, J. D.; Trofymuk, O.; Navrotsky, A.; Lobo, R. F.; Vlachos, D. G. Kinetic and thermodynamic studies of silica nanoparticle dissolution. *Chem. Mater.* **2007**, *19*, 4189–4197.

(40) Mahon, E.; Hristov, D. R.; Dawson, K. A. Stabilising fluorescent silica nanoparticles against dissolution effects for biological studies. *Chem. Commun.* **2012**, *48*, 7970–7972.